Available online at www.sciencedirect.com
ScienceDirect
Journal of Bionic Engineering 14 (2017) 746–758

Comparison of Aerodynamic Forces and Moments Calculated by Three-dimensional Unsteady Blade Element Theory and Computational Fluid Dynamics

Loan Thi Kim Au, Hoang Vu Phan, Hoon Cheol Park

Department of Advanced Technology Fusion and Artificial Muscle Research Center, *Konkuk University*, *Seoul*, *Korea*

Abstract

In previous work, we modified blade element theory by implementing three-dimensional wing kinematics and modeled the unsteady aerodynamic effects by adding the added mass and rotational forces. This method is referred to as Unsteady Blade Element Theory (UBET). A comparison between UBET and Computational Fluid Dynamics (CFD) for flapping wings with high flapping frequencies (>30 Hz) could not be found in literature survey. In this paper, UBET that considers the movement of pressure center in pitching-moment estimation was validated using the CFD method. We investigated three three-dimensional (3D) wing kinematics that produce negative, zero, and positive aerodynamic pitching moments. For all cases, the instantaneous aerodynamic forces and pitching moments estimated via UBET and CFD showed similar trends. The differences in average vertical forces and pitching moments about the center of gravity were about 10% and 12%, respectively. Therefore, UBET is proven to reasonably estimate the aerodynamic forces and pitching moment for flight dynamic study of FW-MAV. However, the differences in average wing drags and pitching moments about the feather axis were more than 20%. Since study of aerodynamic power requires reasonable estimation of wing drag and pitching moment about the feather axis, UBET needs further improvement for higher accuracy.

Keywords: blade element theory, unsteady, computational fluid dynamics, flapping wings, biomimetic

doi: 10.1016/S1672-6529(16)60440-7

1 Introduction

For more than a century, insects' extraordinary flight ability has attracted the attention of biologists and scientists. Recently, insect-mimicking Flapping-Wing Micro Air Vehicles (FW-MAVs) have become an active area of research due to their great potential in various civil and military applications[1]. Flapping-wing MAV development requires a reasonable estimation of the aerodynamic force that is generated by flapping wings, and three standard approaches have been used for this purpose. The first approach measures the time course of the force during a stroke. Although the flight force on the entire body of an insects/MAV has been successfully captured[2–6], it is difficult to distinguish the inertial forces of the wing mass from the aerodynamic forces, making such measurements hard to interpret. The second approach is to compute the aerodynamic forces via Computational Fluid Dynamics (CFD) by solving the Navier-Stokes equations[7–16]. However, a converged solution requires expensive, time-consuming computations, making this a non-optimal approach to analyze the stability and control in FW-MAVs.

A simpler approach based on Blade Element Theory (BET) was suggested in order to overcome these difficulties. This approach is desirable because it can estimate the aerodynamic force in much less time when compared to CFD, enabling parametric study for design of a flapping-wing MAV. However, it is challenging to build an aerodynamic model for BET to reasonably estimate aerodynamic force produced by the flapping wing. BET is based on quasi-steady aerodynamics and has been extensively used in various engineering applications, such in the design and analysis of helicopter blades and wind/tidal turbine blades. Nevertheless, a direct application of conventional BET for flapping

Corresponding author: Hoon Cheol Park
E-mail: hcpark@konkuk.ac.kr

wings is quite far from a reasonable estimation. The conventional steady-state theory could not explain the large lift generated in small insects because flapping flight is heavily affected by unsteady aerodynamic phenomena that are outside the realm of conventional BET.

In a review of the literature on insect flight, based on a wide survey of data available at that time, Ellington showed that in most cases, existing quasi-steady theory failed to calculate a sufficient amount of lift required for hovering[17]. He further suggested that the conventional BET should be modified including the effect of wing rotation as well as other unsteady mechanisms that might be relevant. After Ellington's review, many underlying aerodynamic mechanisms that might explain the large forces produced by flapping wings have been revealed. These include clap-and-fling[12,13,18–20], leading edge vortex created by delayed stall[21–23], rotational circulation and wake capture functioning during stroke reversal[24,25], wing-wake interaction[26], wing-wing interaction[27], and added mass[28,29]. Dickinson *et al*. measured the lift and drag coefficients on a dynamically-scaled model of the fruit fly (*Drosophila*), providing data to estimate the translational force[24]. With these discoveries, BET model could be revised to produce a more appropriate estimation of the aerodynamic force generated by flapping wings.

Sane *et al*.[25] quantitatively characterized the role of wing rotation and thus proposed a revised aerodynamic model of flapping flight that includes the rotational force, translational force and added mass force. This model was used to estimate the aerodynamic force generated by a dynamically-scaled model of a fruit fly (*Drosophila*)[25] and insect-like flapping-wing MAVs[30,31]. However, the aerodynamic model used in these works is not a full three-dimensional (3D) model, i.e. when calculating the added mass force, the wing motion was simplified as being two-dimensional (2D). Hence, in an attempt to improve the accuracy of the force estimation by BET, Truong *et al*. developed a BET model that takes into account the full 3D motion of the wing and includes the unsteady aerodynamic effects of the added mass and rotational forces[32]. Similar to strip theory[33], the modified BET[32] uses concept of gust response suggested by Theodorsen[34] to predict the gust-dependent unsteady aerodynamic force that drew researchers' attention in the beginning of the 20th century[34–36]. Thus, the model is referred to as Unsteady Blade Element Theory (UBET).

In Ref. [32], the calculation by UBET was compared with measured lift and drag in Ref. [25]. The comparison was fair because the robotic fly operated with a wing beat frequency as low as 145 mHz. With such low flapping frequency, the wings' inertia has an insignificant effect on the force measurement. Thus, the measured force represents almost only the aerodynamic component, making a fair comparison of the aerodynamic forces between UBET and the experiment. However, many insects and insect-mimicking FW-MAVs operate at much higher flapping frequencies[37–39]. The flapping frequencies of these flapping-wing systems are often greater than 20 Hz. At such high frequencies, the inertial force due to wing mass is large, which heavily affects the time courses of measured force. Although there were efforts to subtract the inertial force from the total force on flapping wings[40,41], the contamination by the inertial force is inevitable. Moreover, the vibration of the measurement devices due to high flapping frequency is another source of error. As a result, the time course of aerodynamic force estimated by UBET has been never successfully validated by measurement for high flapping frequency.

For validation of UBET, CFD method that only computes the aerodynamic force is preferable to experimental mean. However, there has been no work attempting to compare UBET results with CFD ones. In the present paper, we report the first effort to validate UBET using CFD for a twisted wing with high flapping frequency (38.5 Hz), which is corresponding to a Reynolds number of approximately 10,000. This work is a backup for previous publication (see Ref. [32]), in which UBET was only partly validated with measured forces (Ref. [25]) due to lack of CFD data at that time. In the absence of inertial force, the comparison may give an insight for the development of UBET, as well as providing references for CFD code developers. For the calculation of forces produced by flapping wings, three wing kinematics producing negative, almost zero, and positive pitching moment were considered. Aerodynamic forces and pitching moments generated by these wing kinematics were estimated using both methods. Their time courses and average values were compared for the validation.

2 Materials and methods

2.1 Wing kinematics

Fig. 1 shows the 3D wing motion of the left wing and the wing section with a thickness of dr. The wing section rotates around a feather axis which instantaneously revolves around a flapping axis. In the current FW-MAV[42], the flapping axis is fixed to the body frame, the feather axis aligns on the leading edge of the wing and moves in the stroke plane. An orthogonal coordinate system $Oxyz$ fixed to the body of the FW-MAV and a local coordinate system $\xi\eta\zeta$ fixed to the wing section are used to define the wing motion. The origin O is based at the pivot point of the wing. The x-axis is normal to the longitudinal mid-plane and point to the left. The y-axis is aligned in the stroke plane, parallel to the longitudinal mid-plane of the FW-MAV and points backward. The z-axis aligns with the flapping axis. The ξ-axis aligns with the feather axis. The η-axis is normal to the feather axis and aligned in the stroke plane. Hence, the ζ-axis is parallel to the flapping axis.

The orientation of a wing section is determined as follows. The position of the feather axis is decided by the angle between the feather axis (ξ-axis) and the x-axis, namely, flapping angle ψ. Each wing section is modeled as a straight line whose orientation is determined by the rotation angle θ_r between the wing section and the η-axis.

The three wing kinematics as input for both UBET and CFD were generated using the FW-MAV presented in Ref. [42]. To adjust the pitching moment generated by the FW-MAV, the mechanism could change the range of the flapping angle and thus adjust the aerodynamic center of the produced force. The top view of the CAD model is shown in Fig. 2. The flapping axis (O_3) is attached to the pinion-rocker that rotates about a fixed axis O_4. By moving the rack forward or backward, the position of the flapping axis O_3 can be adjusted to change the flapping angle range. As shown in Fig. 2c, when the rack moves forward, the flapping axis O_3 is shifted backward, resulting in pitching down moment; vice versa, when the rack moves backward, the flapping axis is shifted forward (Fig. 2d), resulting in pitching up moment. The position of O_3 is determined by the rocker angle χ – the angle between the line O_4O_3 and the reference line normal to the longitudinal mid-plane of the body frame.

Three flapping angle ranges corresponding to three values of χ were considered: −66° to 45° (χ = −10°, nose-up case), −50° to 50° (χ = 0°, normal case), and −30° to 63° (χ = 20°, nose-down case). The wing kinematics for the three values of χ were measured at the flapping frequency (f) of 38.5 Hz[42]. For each case of χ, the flapping angles (ψ) and the rotation angles at three wing-span positions, namely 0.25R, 0.5R and 0.75R, were acquired by analyzing images taken with high-speed cameras. Further details of the measurements pertaining to the wing kinematics are given in Ref. [32]. The measured wing kinematics were fitted by three-term sinusoidal functions, e.g.,

$$\psi = a_0 + \sum_{i=1}^{3}\left[a_i \sin\left(2\pi i f t\right) + b_i \cos\left(2\pi i f t\right)\right],$$

where a_0, a_i, b_i (i = 1~3) are fitting coefficients obtained from Curve Fitting Toolbox in MATLAB. The fitted wing kinematics is shown in Fig. 3. In the current flapping-wing mechanism, the wing section at the wing root is aligned with the flapping axis (Fig. 1), thus the rotation angle at the wing root is 90°. The rotation angle at the wing tip was linearly extrapolated from those at 50% and 75% of the wing span. Then the rotation angle of a wing section was approximated using the cubic spline interpolation.

2.2 Unsteady Blade Element Theory (UBET)

In BET the wing is divided into infinitesimal wing sections, and each wing section is considered as a two-dimensional airfoil. The aerodynamic forces acting on all wing sections are integrated to calculate the force produced by the wing. In the current UBET, the rotational and added mass forces that represent the unsteady

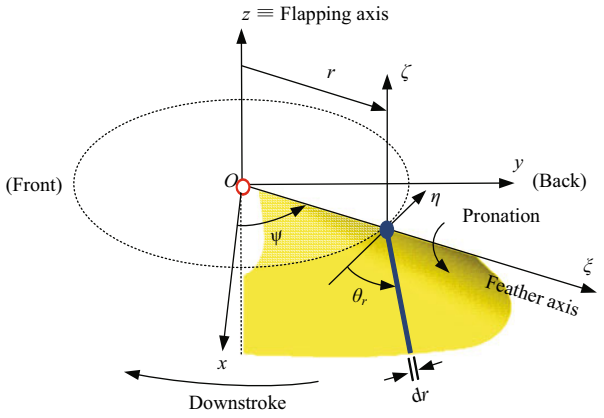

Fig. 1 Motion of the left wing and parameters describing the wing kinematics. The thick blue line indicates a wing section. The hollow circle indicates the wing's pivot point.

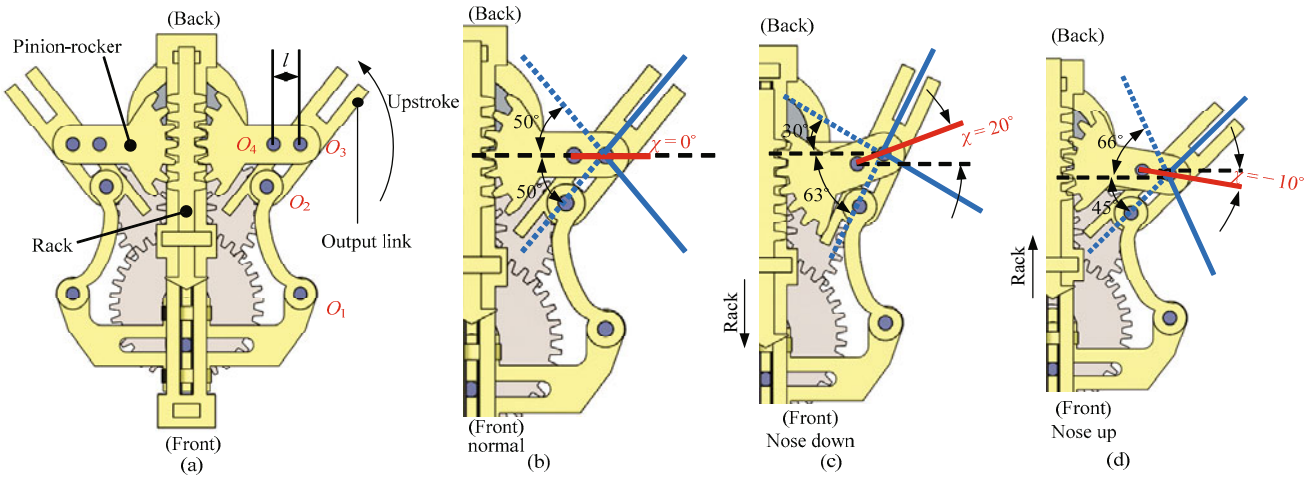

Fig. 2 Top view of the CAD model of the FW-MAV. (a) Rack-and-pinion mechanism to change the flapping angle range[42]. The length of O_4O_3 (l) is 0.98 mm. (b–d) Flapping angle ranges corresponding to various positions of the rack (taken from Table 2 in Ref. [42]).

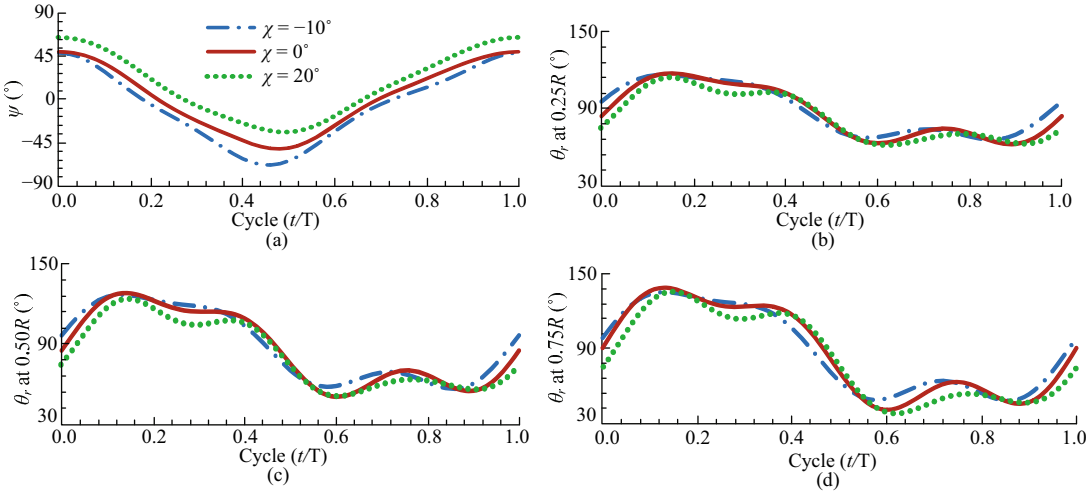

Fig. 3 Time courses of wing kinematics corresponding to three positions of the rack. (a) Flapping angle; (b–d) rotation angles at 25%, 50% and 75% wing span, respectively.

effects are included in addition to the translational force corresponding to the steady state. These three force components are summed up to acquire the total aerodynamic force produced by the flapping wing. Since the UBET was detailed in Ref. [32], we just briefly explain each of the force components in the subsections below.

2.2.1 Translational force

The translational force acting on a wing section during upstroke with chord length c is illustrated in Fig. 4. The wing section is moving with velocity $V_T = |r\dot{\psi}|$. The geometric Angle of Attack (AoA) of the wing section, denoted by θ, can be determined based on the rotation angle θ_r. If the wing section moves in the positive direction of the η-axis (upstroke), θ is identical to θ_r, otherwise, θ equals to $\pi - \theta_r$. The symbol V_i stands for the induced velocity, and V is the inflow velocity.

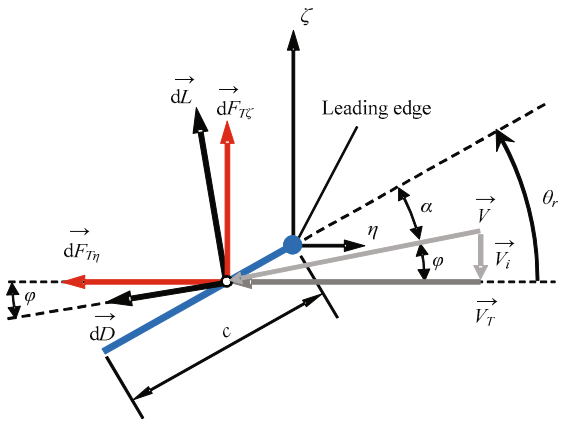

Fig. 4 Translational force on a wing section. The terms "dL" and "dD" stand for lift and drag on the wing section due to translational motion.

The lift and drag are determined by the effective AoA (α). The lift and drag coefficients (C_{L} and C_{D}) for a flat wing at a low Reynolds number were measured in Ref. [24]. Since the translational speed and the Reynolds number were low (0.25 $\mathrm{m\cdot s^{-1}}$ and 192, respectively), we assumed that the geometric AoA and effective AoA in Ref. [24] were similar. In the current study, to acquire the effective AoA, we combined the blade element theory and the momentum theory to obtain the following equations:

$$\frac{c(r)}{4\Psi_F r}\sqrt{\left(\frac{V_i}{V_T}\right)^2+1}\left[C_{\mathrm{L}}(\alpha)-C_{\mathrm{D}}(\alpha)\frac{V_i}{V_T}\right]-\left(\frac{V_i}{V_T}\right)^2=0,\Psi, \tag{1}$$

$$\alpha=\theta-\tan^{-1}\left(\frac{V_i}{V_T}\right), \tag{2}$$

where Ψ_F is the flapping amplitude. By solving the coupled Eqs. (1) and (2), we acquired α and V_i, then obtained C_{L} and C_{D}. The translational force is decomposed into the ζ- and η-axes as:

$$\mathrm{d}F_{T\zeta}=\frac{\rho}{2}c\left[C_{\mathrm{L}}\cos\varphi-C_{\mathrm{D}}\sin\varphi\right]\left(V_i^2+V_T{}^2\right)\mathrm{d}r, \tag{3}$$

$$\mathrm{d}F_{T\eta}=\left[C_{\mathrm{L}}\sin\varphi+C_{\mathrm{D}}\cos\varphi\right]\frac{\rho}{2}\left(V_i^2+V_T{}^2\right)c\mathrm{d}r$$

during downstroke, (4)

$$\mathrm{d}F_{T\eta}=-\left[C_{\mathrm{L}}\sin\varphi+C_{\mathrm{D}}\cos\varphi\right]\frac{\rho}{2}\left(V_i^2+V_T{}^2\right)c\mathrm{d}r$$

during upstroke, (5)

where φ is the induced AoA, and ρ denotes the air density (1.225 $\mathrm{kg\cdot m^{-3}}$).

2.2.2 Added mass force

When the wing accelerates, it encounters a reaction force due to the accelerated air. Similar to the models in Refs. [25,30–32], we assumed that the accelerated air around the wing section is a cylinder with a diameter of the chord length and a height of thickness dr, as shown in Fig. 5a. The added mass force acting on a wing section is illustrated in Fig. 5b and is expressed as:

$$\overrightarrow{\mathrm{d}F_A}=-\frac{\pi}{4}\rho c^2\overrightarrow{a_n}\mathrm{d}r, \tag{6}$$

where $\vec{a}_n=a_n\left(-\cos\theta_r\vec{e}_\zeta+\sin\theta_r\vec{e}_\eta\right)$ is the acceleration of the air in the direction normal to the wing section ($\vec{e}_\zeta$ and $\vec{e}_\eta$ are unit vectors, i.e. $\left|\vec{e}_\zeta\right|=1,\left|\vec{e}_\eta\right|=1$, in the ζ- and η-axes, respectively). The term a_n is expressed as:

$$a_n=r\ddot{\psi}\sin\theta_r+\frac{c}{2}\dot{\psi}^2\cos\theta_r\sin\theta_r+\frac{c}{2}\ddot{\theta}_r. \tag{7}$$

In Eq. (7), the second term of a_n includes $\dot{\psi}^2$ which does not appear in Refs. [25,30,31], in which the motion of the wing section is simplified as two-dimensional. The added mass force is decomposed in the ζ- and η-axes as:

$$\mathrm{d}F_{A\zeta}=\frac{\pi}{4}\rho c^2a_n\cos\theta_r\mathrm{d}r, \tag{8}$$

$$\mathrm{d}F_{A\eta}=-\frac{\pi}{4}\rho c^2a_n\sin\theta_r\mathrm{d}r. \tag{9}$$

2.2.3 Rotational force

The rotational force acts normal to the wing section, as shown in Fig. 6. The expression for the rotational force is as:

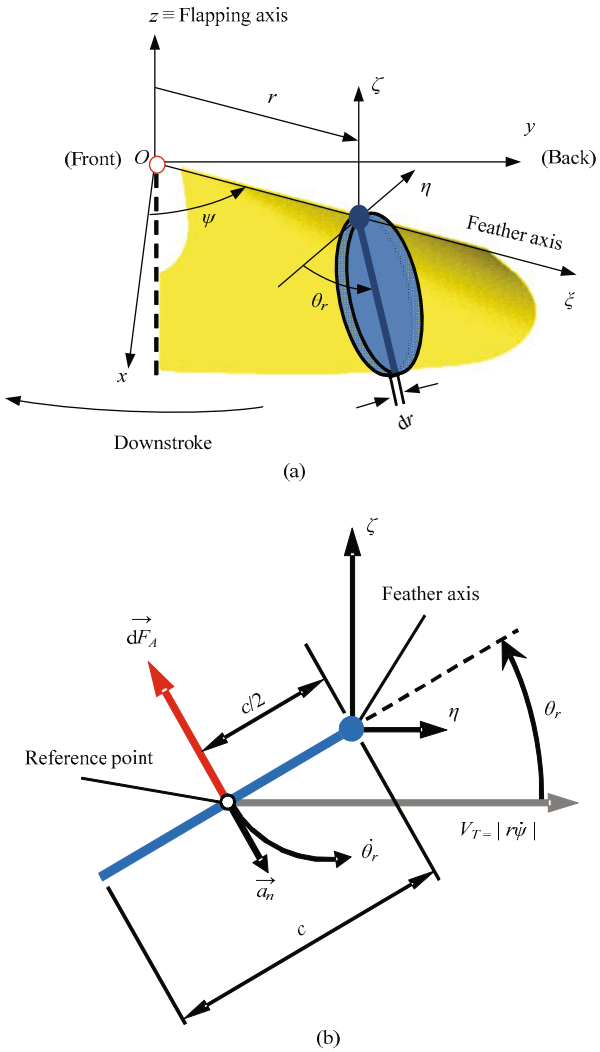

Fig. 5 (a) Accelerated air around a wing section; (b) added mass force.

$$\mathrm{d}F_{\mathrm{rot}} = \rho V_T c_{\mathrm{rot}} \dot{\theta}_r c^2 \mathrm{d}r, \tag{10}$$

where c_{rot} is the rotational force coefficient. According to Ref. [25], c_{rot} is a function of the non-dimensional rotational velocity, which is expressed as:

$$\bar{\omega} = \frac{\dot{\theta}_r \bar{c}}{U_t}, \tag{11}$$

where $\bar{c}$ is the mean chord and U_t is the wing tip velocity expressed as $U_t = |R\dot{\psi}|$, where R stands for wing span. In Ref. [25], the dependency of c_{rot} on $\bar{\omega}$ was measured for a range of $\bar{\omega}$ from 0.166 to 0.374. When $\bar{\omega}$ increases, the measured c_{rot} tends to reach the predicted value given by:

$$c_{\mathrm{rot}} = \pi\left(0.75 - \frac{x_f}{c}\right), \tag{12}$$

where x_f is the distance from the feather axis to the leading edge. Because the feather axis in our FW-MAV is attached to the leading edge, $x_f = 0$. In the current UBET, we used the theoretical constant given in Eq. (12) despite the fact that c_{rot} may be a function of $\bar{\omega}$. The rotational force is decomposed into ζ- and η-axes as:

$$\mathrm{d}F_{R\zeta} = \mathrm{d}F_{\mathrm{rot}} \cos\theta_r \mathrm{d}r, \tag{13}$$

$$\mathrm{d}F_{R\eta} = -\mathrm{d}F_{\mathrm{rot}} \sin\theta_r \mathrm{d}r. \tag{14}$$

2.2.4 Pitching moment

The pitching moments due to translational force, added mass force and rotational force are summed up to acquire the total aerodynamic pitching moment generated by the flapping wing. Han *et al*. measured the pitching moment due to the translational force on a dynamically scaled-up robotic hawkmoth wing, and proved that the center of pressure of translational force moves depending on the angle of attack[41]. In Ref. [41], the feather axis of the wing was located at 19.5% chord length, the translational pitching moment coefficient was measured about this axis and expressed as:

$$C_{M,0.195c} = 1.451\sin\theta\cos\theta - 1.256\sin\theta, \tag{15}$$

where θ is the geometric AoA. By definition in Ref. [41], $C_{M,0.195c}$ is positive if it pitches up the wing section, as shown in Fig. 7. In the current FW-MAV, the feather axis is attached to the leading edge, hence, the pitching moment about the feather axis is expressed as Eqs. (16) and (17).

For added mass force and rotational force, we assumed that the centers of pressure of these forces are located at 1/2*c*.

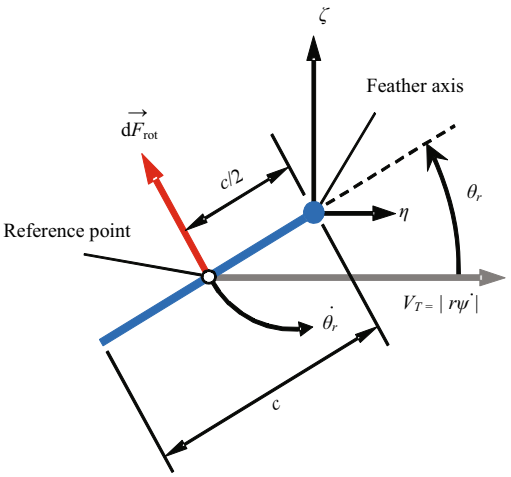

Fig. 6 Rotational force on a wing section.

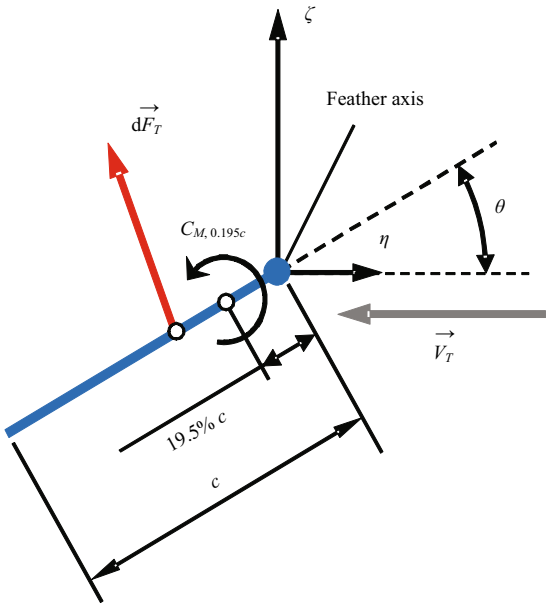

Fig. 7 Pitching moment due to translational force on a wing section of the left wing during upstroke.

$$\mathrm{d}M_{T\xi} = -C_{M,0.195c}\frac{\rho}{2}(r\dot{\psi})^2 c^2 \mathrm{d}r + 0.1946c\left(F_{T\zeta}\cos\theta + F_{T\eta}\sin\theta\right) \text{ during downstroke,} \tag{16}$$

$$\mathrm{d}M_{T\xi} = C_{M,0.195c}\frac{\rho}{2}(r\dot{\psi})^2 c^2 \mathrm{d}r - 0.1946c\left(F_{T\zeta}\cos\theta - F_{T\eta}\sin\theta\right) \text{ during upstroke.} \tag{17}$$

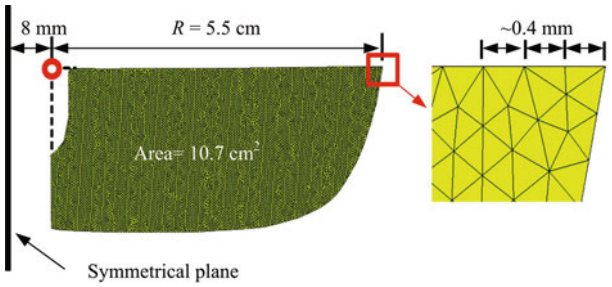

Fig. 8 Wing planform. The hollow circle indicates the pivot point.

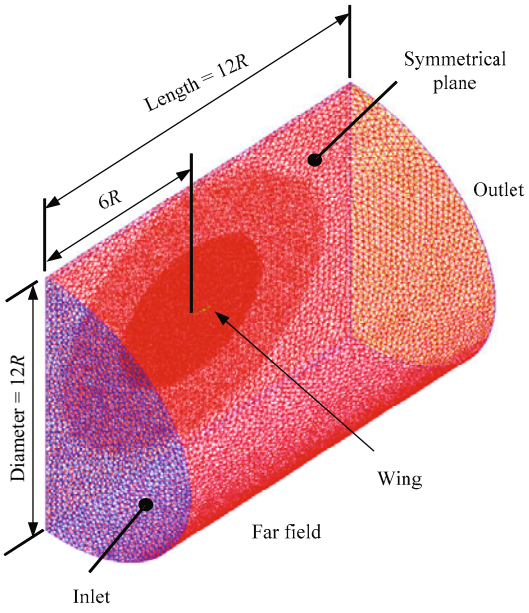

Fig. 9 Computational domain.

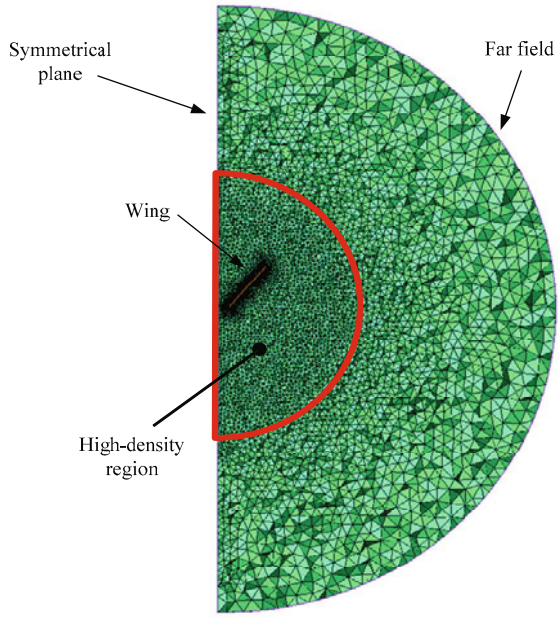

Fig. 10 Cross section of the computational domain.

2.3 Computational fluid dynamics

2.3.1 Computational domain and boundary condition

The wing is modeled as a membrane twisted from the root to tip. The wing planform is shown in Fig. 8. The pivot point of the wing is based at the wing root, aligned on the leading edge. Because of the longitudinal symmetrical plane, the CFD model was built for only left wing. Thus, the computational domain is a half cylinder with a diameter and a length of 12 times the wing span R, as shown in Fig. 9. A symmetrical plane which models the longitudinal mid-plane of the FW-MAV was imposed parallel to the yz plane at a distance of 8 mm from the pivot point. Note that with the "symmetry" boundary type assigned to the symmetrical plane, Fluent can simulate the wing-wing interaction between the left and the right wings, although the effect of this unsteady mechanism is weak for the current study because the flapping angle is not large enough. At the inlet, outlet and far field, the flow velocity is set to 0.

2.3.2 Grid and computational solver

The grid was generated by the commercial meshing software ANSYS ICEM CFD 16.2. The wing surface was meshed into about 21,000 triangles with element edge lengths of about 0.4 mm (see Fig. 8). The grid is the finest around the wing and becomes coarser toward the far-field region, as shown in Fig. 10. The volume mesh is filled by about 3.8 million tetrahedrons. A high-density region with a radius of double the wing span was built around the wing. Inside this region, the minimum edge length is 0.4 mm at the cell layer around the wing, and the maximum is 2 mm toward the boundary of the region. The tetra growth rate away from the high-density region is 1.1.

The flow was computed by the commercial software ANSYS Fluent 16.2. The wing motion was simulated using the dynamic mesh feature with a user-defined function. In the current study, since the rotation angles of the wing sections change from root to tip, the wing is twisted. In other words, the wing does not only move but also deforms over the flapping cycle. To describe the wing motion for such a case, a DEFINE_GRID_MOTION macro was used to update node positions on the wing mesh based on the wing kinematical data plotted in Fig. 3. At each time step, the cells are deformed or remeshed to accommodate for the motion of the wing. We used an incompressible laminar model for

the flow. The spatial and time discretizations were set to second-order. The semi-implicit method for pressure-linked equations (SIMPLE) algorithm was used as the solver, and the time step was set to 1/1000 of a flapping cycle.

2.3.3 Grid-independence test

The number of elements in a grid depends on two parameters: the maximum element edge length on the wing surface, denoted by s_1, and the maximum element edge length in the high-density region, denoted by s_2. Three grids corresponding to three pairs of s_1 and s_2 were considered. Their data are shown in Table 1. The results calculated for $\chi = 0^\circ$ in the first cycle using the three grids are plotted in Fig. 11. Although the computation for the first cycle is not the converged solution because the flow is not settled, the similarity in the calculation for the three grids implies that the converged solutions are also similar when the flow becomes periodic in the following flapping cycles for the three grids. We defined the wing lift (L) as the force component normal to the stroke plane, the wing drag (D) as the force component in the stroke plane and normal to the wing span, and M_f as the wing pitching moment (pitching moment about the feather axis). In other words:

$$L = F_\zeta = F_z, \tag{18}$$

$$D = F_\eta, \quad M_f = -M_\xi \text{ during downstroke}, \tag{19}$$

$$D = -F_\eta, \quad M_f = M_\xi \text{ during upstroke}. \tag{20}$$

These forces and moment were normalized as $L^+ = 2L/(\rho U^2 S)$, $D^+ = 2D/(\rho U^2 S)$, and $M_f^+ = 2M_f/(\rho U^2 S\bar{c})$, respectively, where U is the mean velocity at the radius of the second moment of wing area (r_2 = 30.0 mm) expressed as $U = 2\Psi_F r_2 f = 4.08\,\mathrm{m\cdot s^{-1}}$, S is the wing area and $\bar{c}$ is the mean chord length. Except for slight differences in the force peaks, the time courses computed for the three grids were similar. Therefore, it was concluded that grid 3 with 3.8 million elements was appropriate for the present study.

2.3.4 Validation of ANSYS Fluent

Meng and Sun computed aerodynamic forces in hovering fruitflies using their in-house code[43]. We reproduced the calculation using ANSYS Fluent. The calculation by the in-house code and by ANSYS Fluent are plotted in Fig. 12. Because pitching moment was not considered in Ref. [43], only data on wing lift and wing drag are shown. In this validation, we used grid with similar number of elements as grid 3 mentioned above. There are slight differences in the force peaks due to difference in wing shape (Meng and Sun[43] modeled the wing as flat plate with thickness of 0.03 mean chord length and rounded leading and trailing edges; the wing used in ANSYS Fluent is modeled as a membrane). However, the results calculated by ANSYS Fluent agree well with the computation by the in-house code.

Table 1 Sizes of three tested grids

	s_1 (mm)	s_2 (mm)	No. elements on the wing	Total no. elements
Grid 1	0.8	4	~6,000	~1 million
Grid 2	0.6	3	~9,000	~1.8 million
Grid 3	0.4	2	~21,000	~3.8 million

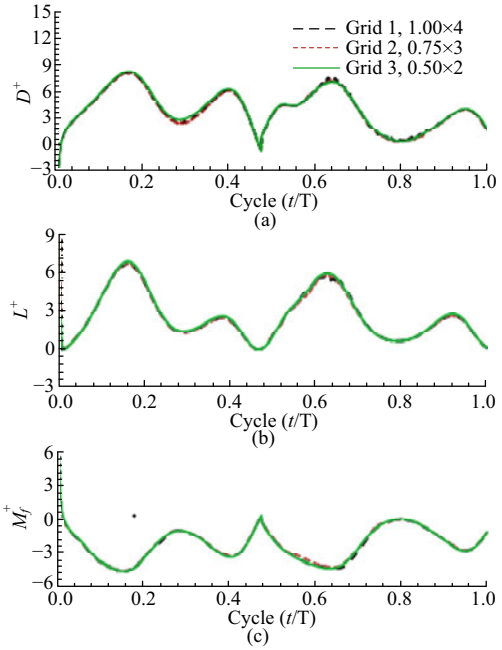

Fig. 11 Forces and moment computed by ANSYS Fluent using the three grids. (a) Non-dimensional drag $\left(D^+\right)$; (b) non-dimensional lift $\left(L^+\right)$; (c) non-dimensional pitching moment about the feather axis $\left(M_f^+\right)$.

3 Results and discussion

3.1 Lift, drag and pitching moment about the feather axis

For each set of wing kinematics, it took about 10 days for CFD to complete the computation for 6 cycles

using a personal computer (64-bit operating system, Intel® Core™ i7-3770 CPU 3.40 GHz, RAM 32 GB). In contrast, it only took about 2 minutes for UBET to complete calculation for one set of wing kinematics. For all cases, the unsteady forces and moments obtained by CFD reached an almost periodic state after 3 flapping cycles.

The time courses of non-dimensional lift, drag and pitching moment about the feather axis for $\chi = -10^{\circ}$, 0° and 20° are plotted in Fig. 13. The normalized angular velocities are expressed as: $\dot{\psi}^{+} = \dot{\psi} / f$ and $\dot{\theta}_r^{+} = \dot{\theta}_r / f$ (f is the flapping frequency). The rotation angle θ_r and rotating rate $\dot{\theta}_r$ are average values from three wing-span positions: 25%R, 50%R and 75%R. For CFD, the time courses are taken at the fifth cycle when the flows completely become periodic. At the end of each half stroke, the definition of positive drag and pitching moment reverses as defined in Eqs. (19) and (20), which explains the sudden jump in the time courses of D^{+} and M_f^{+} at t/T=0.455, 0.478 and 0.492 for $\chi = -10^{\circ}$, 0° and 20°, respectively. For UBET, from the beginning of each half stroke, the wing quickly pitches down, the geometry AoA decreases from about 90° to about 60° in $\Delta t / T \approx 0.12$ (Figs. 13a, 13e, 13i), resulting in negative rotational component and positive added mass component. The negative rotational component causes a sudden decrease in D+ (Figs. 13b, 13f, 13j) and an increase in M_f^{+} near the beginning of each half stroke (Figs. 13d, 13h, 13l), which does not appear in estimation by CFD. Near the end of each half stroke, the wing quickly pitches up, generating positive rotational force and negative added mass force. The negative added mass force is dominant during this period, leads to sharp decrease in total drag and augments the total pitching moment.

The time-course lift estimated by UBET shows good agreement with the estimation by ANSYS Fluent (Figs. 13c, 13g, 13k). For drag and pitching moment, the time histories show similar trends between UBET and CFD except for the short period of stroke reversals, which requires an unsteady model for wing-wake interaction. Although UBET over estimated the added mass drag at stroke reversals (Figs. 13b, 13f, 13j), the contribution of this force component enhances the agreement between UBET and CFD in most of the flapping cycle, which only summation of translational and rotational components could not achieve.

The mean L^{+}, D^{+} and M_f^{+} computed by UBET and CFD are summarized in Table 2 for comparison. The mean values for CFD were taken at the fifth cycle. The difference in lift between UBET and CFD is about 10%. Meanwhile, the differences in wing drag and pitching moment about the feather axis are more than 20%. These observations show that the current UBET can provide reasonable estimation in lift. However, its accuracy in estimating wing drag and pitching moment about the feather axis is relatively poor. Wing drag and pitching moment about the feather axis relate directly to the aerodynamic input power. Hence, the current UBET needs to be modified for study of power efficiency in FW-MAV.

3.2 Forces and pitching moment for design of FW-MAV

For design of FW-MAVs, the forces and moments in the coordinate system $Oxyz$ fixed to the body frame are important. These forces and moments relate directly to flight dynamic studies, and determine whether the FW-MAV can perform a certain maneuver (hovering, cruise, takeoff, *etc*.) or not. For example, in hovering flight, the vertical force must balance the weight of the FW-MAV, and the horizontal force and pitching moment about the Center of Gravity (CG) must be zero. For the current FW-MAV, because of the longitudinal

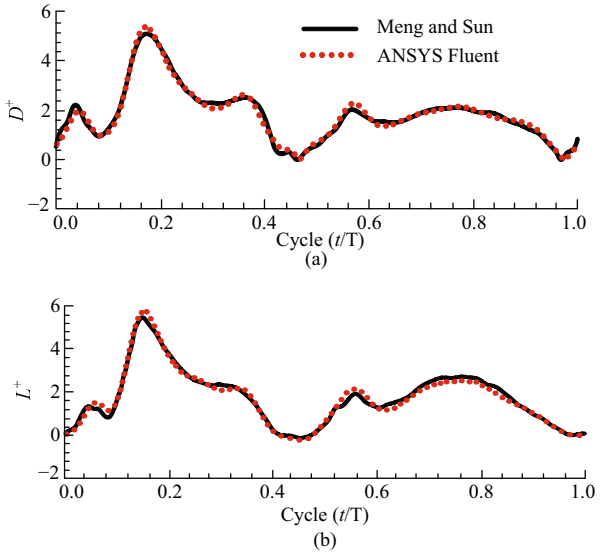

Fig. 12 Non-dimensional lift (a) and drag (b) computed by the in-house code[43] and by ANSYS Fluent. The results from in-house code are taken from Figs. 11c, 11d in Ref. [43]. The results from ANSYS Fluent are taken at the 3rd flapping cycle when the flow becomes periodic.

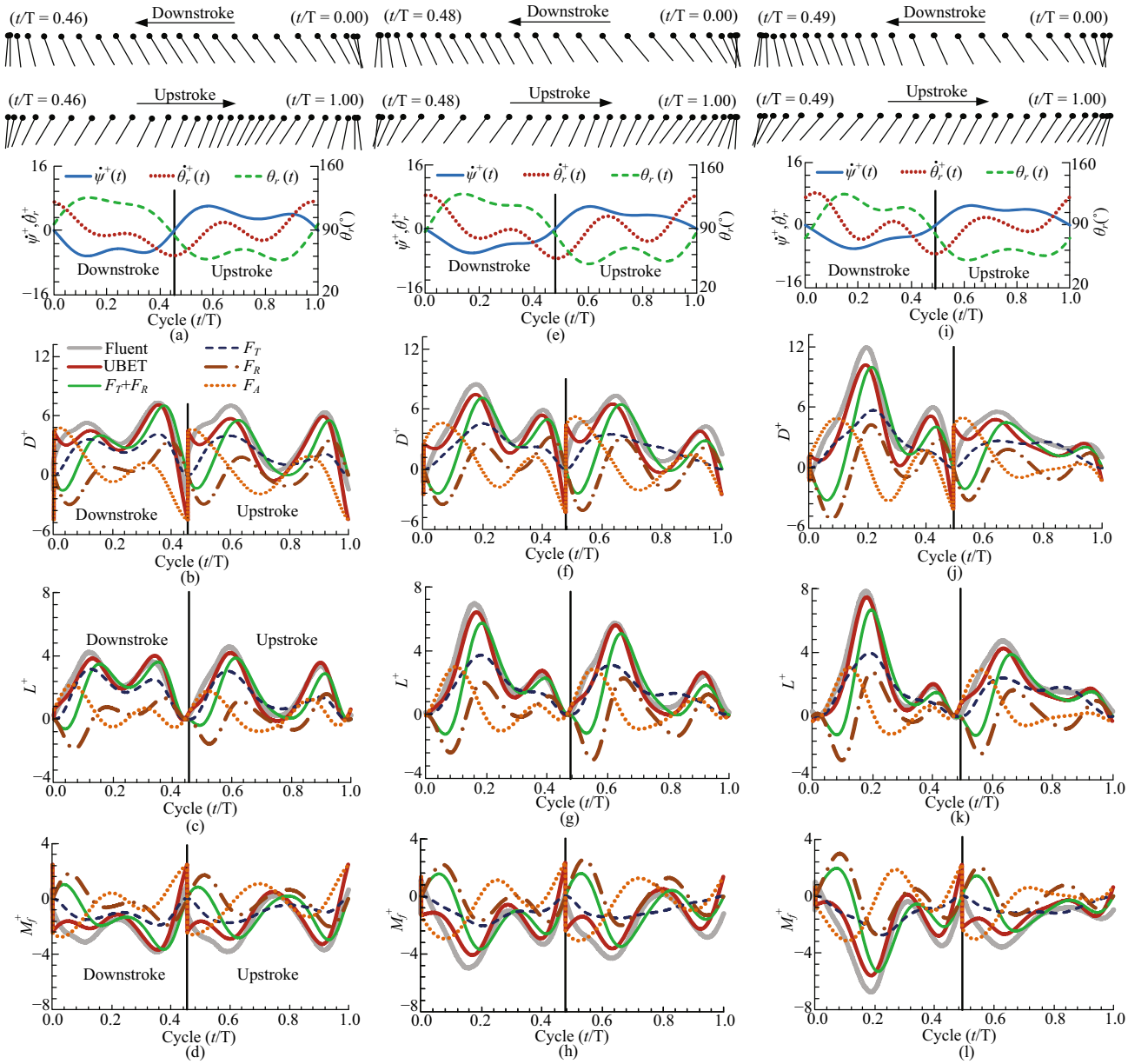

Fig. 13 Wing motion data (the orientation of the wing section is shown above the plot), time courses of D^+, L^+, and M_f^+ for (a–d) $\chi = -10^\circ$, (e–h) $\chi = 0^\circ$, and (i–l) $\chi = 20^\circ$.

symmetrical plane, the motion in the lateral mode is canceled out, thus only longitudinal mode was considered. We defined Y and Z as force components in the y- and z-axes, and M as the pitching moments about the CG. Since the stroke plane is horizontal, Y and Z are identical to the horizontal and vertical forces, respectively. These quantities are normalized as:

$$Y^+ = \frac{2Y}{\rho U^2 S}, Z^+ = \frac{2Z}{\rho U^2 S}, M^+ = \frac{2M}{\rho U^2 S\bar{c}}. \quad (21)$$

Note that Z^+ is identical to L^+. The time courses of this component are already plotted in Fig. 13. Time courses of Y^+ and M^+ computed by UBET and CFD are plotted in Fig. 14. The coordinates of CG were defined as $y = 0$ and $z = -7.2$ mm, i.e., directly below the pivot point. The time histories show similar trends between UBET and CFD, and the differences between UBET and CFD are observed during the stroke reversals.

The average Y^+, Z^+, and M^+ computed by UBET and CFD are given in Table 3 for comparison. In all cases, the differences in Z^+ between UBET and CFD are about 10%. The percentage differences in the Y^+ are

Table 2 Average normalized lift, drag and pitching moment about the feather axis

Case	Mean	UBET	ANSYS Fluent	Difference
$\chi = -10^\circ$	L^+	2.04	2.19	−6.9%
	D^+	3.23	4.08	−20.8%
	M_f^+	−1.63	−2.13	23.3%
$\chi = 0^\circ$	L^+	2.16	2.45	−11.7%
	D^+	3.16	4.06	−22.3%
	M_f^+	−1.64	-2.21	26.0%
$\chi = 20^\circ$	L^+	2.05	2.34	−12.4%
	D^+	3.13	4.19	−25.3%
	M_f^+	−1.62	−2.28	28.6%

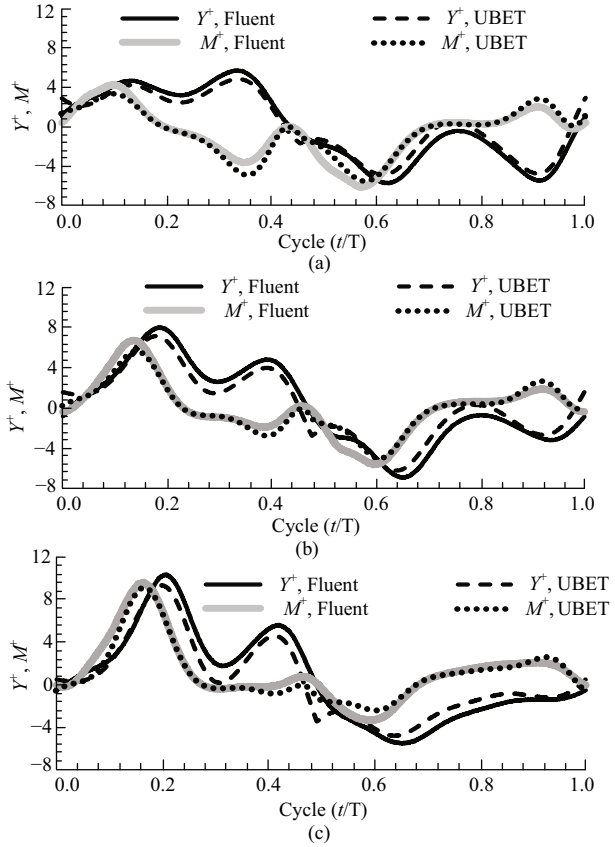

Fig. 14 Time courses of Y^+ and M^+ for (a) $\chi = -10^\circ$, (b) $\chi = 0^\circ$, and (c) $\chi = 20^\circ$.

large, but that is because the force components in the y-axis are close to 0. In all cases, the differences in Y^+ are less than 0.2 (equivalent to 0.4 gf). The differences in the pitching moments are about 12% for the nose-up and nose-down cases. For the normal case where the pitching moments is almost zero, the difference between UBET and CFD is also close to zero (normalized difference is about 0.05, equivalent to 2.2 gf·mm). Through this comparison, we confirmed that UBET can effectively estimate the aerodynamic forces and pitching moment with an acceptable accuracy for design of FW-MAV.

Table 3 Comparison of average forces and pitching moment in the *Oxyz* coordinate system

Case		UBET	ANSYS Fluent	Difference
$\chi = -10^\circ$	Z^+	2.04	2.19	−6.9%
	Y^+	0.18	0.01	–
	M^+	−0.62	−0.56	−10.4%
$\chi = 0^\circ$	Z^+	2.16	2.45	−11.7%
	Y^+	0.30	0.23	–
	M^+	0.01	0.06	–
$\chi = 20^\circ$	Z^+	2.05	2.34	−12.4%
	Y^+	0.4	0.60	–
	M^+	1.04	1.19	−12.3%

The current UBET employs the lift, drag and pitching moment coefficients measured for dynamically scaled robotic wings reported in Ref. [24,25,41]. The differences in wing shape and Reynolds number between the references and the current FW-MAV are the main sources of error in the estimation by the current UBET. For a more accurate estimation, UBET needs accurate C_L, C_D and C_M for the wings that are used for the current FW-MAV. The assumption of pressure center at the half chord for rotation force and added mass force may be another source of error for pitching moment estimation. A detailed investigation on pressure centers of these force components is another direction for improving UBET in the future. Despite these limitations, the agreement between the current UBET and CFD results is reasonable for design stage of FW-MAVs where quick force and moment estimation is required.

4 Conclusion

In this work, we have investigated the accuracy of UBET by conducting a comparison with CFD both in terms of time-course and average estimations. Three wing kinematics corresponding to three cases of pitching moment generation were considered. The forces and pitching moments produced by these three wing kinematics were computed using both UBET and CFD. The comparison showed that in all cases, the time histories of forces and pitching moments exhibited similar trends. The estimations of vertical force, horizontal force and pitching moment about CG obtained with UBET are in good agreement with those obtained by CFD. The av-

erage vertical forces had differences of about 10%. The differences in the average normalized horizontal forces, which were close to zero, were less than 0.2. For the nose-up and nose-down cases, the differences in the average pitching moments about CG were about 12%. For the normal case where the average pitching moments were close to zero, the difference between UBET and CFD was also close to zero. These results confirm the capability of estimating the aerodynamic force and moment for flight dynamic study of FW-MAV with high flapping frequency with acceptable accuracy using UBET. While CFD took at least 10 days to produce the result, UBET took only 2 minutes to achieve the same level of accuracy under the same computational environment. Thus UBET can be useful for design stage of FW-MAVs. However, the accuracy of UBET in estimating wing drag and pitching moment about the feather axis was relatively poor. The differences between UBET and CFD in wing drag and pitching moment about the feather axis were more than 20%. Hence, for study of aerodynamic power which requires reasonable estimation of wing drag and pitching moment about the feather axis, UBET needs further modification.

Acknowledgment

This research was supported by a grant to Bio-Mimetic Robot Research Center (UD130070ID) funded by Defense Acquisition Program Administration and by Agency for Defense Development, and partially supported by the Basic Science Research Program through the National Research Foundation of Korea (NRF) funded by the Ministry of Science, ICT and Future Planning (Grant No. 2013R1A2A2A01067315).

References

[1] Shyy W, Berg M, Ljungqvist D. Flapping and flexible wings for biological and micro vehicles. *Progress in Aerospace Sciences*, 1999, **35**, 455–505.

[2] Nguyen Q V, Truong Q T, Park H C, Goo N S, Byun D. Measurement of force produced by an insect-mimicking flapping-wing system. *Journal of Bionic Engineering*, 2010, **7**, S94–S102.

[3] Morrison C L, Vandenheede R B R, Kumar D, Bernal L P, Cesnik C. Force measurements of a flapping wing with two angular degrees of freedom and bio-inspired kinematics. *Proceedings of the* 50*th AIAA Aerospace Sciences Meeting including the New Horizons Forum and Aerospace Exposition*, Nashville, Tennessee, USA, 2012, 1–8.

[4] Nagai H, Isogai K, Hayase T. Measurement of unsteady aerodynamics forces of 3D flapping wing in hovering to forward flight. *Proceedings of the* 26*th International Congress of the Aeronautical Sciences*, Anchorage, Alaska, USA, 2008, 1–11.

[5] Ştefănescu D M, Butoescu V. Equipment for determining aerodynamic forces on flapping wings. *Proceedings of the* 19*th IMEKO World Congress*, Lisbon, Portugal, 2009, 311–315.

[6] Mueller D, Bruck H A, Gupta S K. Measurement of thrust and lift forces associated with drag of compliant flapping wing for micro air vehicles using a new test stand design. *Experimental Mechanics*, 2010, **50**, 725–735.

[7] Liu H, Ellington C P, Kawachi K, Berg C V D, Willmott A P. A computational fluid dynamic study of hawkmoth hovering. *Journal of Experimental Biology*, 1998, **201**, 461–477.

[8] Zhu L, Peskin C S. Simulation of a flapping flexible filament in a flowing soap film by the immersed boundary method. *Journal of Computational Physics*, 2002, **179**, 452–468.

[9] Sun M, Tang J. Unsteady aerodynamic force generation by a model fruit fly wing in flapping motion. *Journal of Experimental Biology*, 2002, **205**, 55–70.

[10] Tay W B, van Oudheusden B W, Bijl H. Numerical simulation of X-wing type biplane flapping wings in 3D using the immersed boundary method. *Bioinspiration & Biomimetics*, 2014, **9**, 1–21.

[11] Vanella M, Fitzgerald T, Preidikman S, Balaras E, Balachandran B. Influence of flexibility on the aerodynamic performance of a hovering wing. *Journal of Experimental Biology*, 2009, **212**, 95–105.

[12] Miller L A, Peskin C S. A computational fluid dynamics of "clap and fling" in the smallest insects. *Journal of Experimental Biology*, 2005, **208**, 195–212.

[13] Miller L A, Peskin C S. Flexible clap and fling in tiny insect flight. *Journal of Experimental Biology*, 2009, **212**, 3076–3090.

[14] Wang Z J, Birch J M, Dickinson M H. Unsteady forces and flows in low Reynolds number hovering flight: Two-dimensional computations *vs* robotic wing experiments. *Journal of Experimental Biology*, 2004, **207**, 449–460.

[15] Meng X, Liu Y. Aerodynamics of ascending flight in fruit flies. *Journal of Bionic Engineering*, 2017, **14**, 75–87.

[16] Phan H V, Au T K L, Park H C. Clap-and-fling mechanism in a hovering insect- like two-winged flapping-wing micro air vehicle. *Royal Society Open Science*, 2016, **3**, 1–18.

[17] Ellington C P. The aerodynamics of hovering insect flight. I. The quasi-steady analysis. *Philosophical Transactions of the*

Royal Society of London B, 1984, **305**, 1–15.

[18] Weis-Fogh T. Quick estimates of flight fitness in hovering animals, including novel mechanisms for lift production. *Journal of Experimental Biology*, 1973, **59**, 169–230.

[19] Lighthill M J. On the Weis-Fogh mechanism of lift generation. *Journal of Fluid Mechanics*, 1973, **60**, 1–17.

[20] Maxworthy T. Experiments on the Weis-Fogh mechanism of lift generation by insects in hovering flight. Part 1. Dynamics of the 'fling'. *Journal of Fluid Mechanics*, 1979, **93**, 46–73.

[21] Ellington C P, Van Den Berg C, Willmott A P, Thomas A L R. Leading-edge vortices in insect flight. *Nature*, 1996, **384**, 626–630.

[22] Ellington C P. The novel aerodynamics of insect flight: Application to micro-air vehicles. *Journal of Experimental Biology*, 1999, **202**, 3439–3448.

[23] Van Den Berg C, Ellington C P. The vortex wake of a hovering model hawkmoth. *Philosophical Transactions of the Royal Society of London B*, 1997, **352**, 317–328.

[24] Dickinson M H, Lehmann F-O, Sane S P. Wing rotation and the aerodynamic basis of insect flight. *Science*, 1999, **284**, 1954–1960.

[25] Sane S P, Dickinson M H. The aerodynamic effects of wing rotation and a revised quasi-steady model of flapping flight. *Journal of Experimental Biology*, 2002, **205**, 1087–1096.

[26] Birch J M, Dickinson M H. The influence of wing-wake interactions on the production of aerodynamic forces in flapping flight. *Journal of Experimental Biology*, 2003, **206**, 2257–2272.

[27] Lehmann F O, Sane S P, Dickinson M H. The aerodynamic effects of wing-wing interaction in flapping insect wings. *Journal of Experimental Biology*, 2005, **208**, 3075–3092.

[28] Ellington C P. The aerodynamics of hovering insect flight II Morphological parameters. *Philosophical Transactions of the Royal Society of London B*, 1984, **305**, 17–40.

[29] Sane S P, Dickinson M H. The control of flight force by a flapping wing: Lift and drag production. *Journal of Experimental Biology*, 2001, **204**, 2607–2626.

[30] Ansari S A, Zbikowski R, Knowles K. Aerodynamic modeling of insect-like flapping flight for micro air vehicles. *Progress in Aerospace Sciences*, 2006, **42**, 129–172.

[31] Khan Z A, Agrawal S K. Force and moment characterization of flapping wings for micro air vehicle application. *Proceedings of the* 2005 *American Control Conference*, Portland, Oregon, USA, 2005, 1515–1520.

[32] Truong Q T, Nguyen Q V, Truong V T, Park H C, Byun D, Goo N S. A modified blade element theory for estimation of forces generated by a beetle-mimicking flapping wing system. *Bioinspiration & Biomimetics*, 2011, **6**, 1–11.

[33] Schmidt L V. *Introduction to Aircraft Flight Dynamics*, American Institute of Aeronautics and Astronautics, Reston, Virginia, USA, 1998, 397.

[34] Theodorsen T. *General Theory of Aerodynamic Instability and the Mechanism of Flutter*, NACA annual report, 1935, **20**, 413–433.

[35] Wagner H. Über die Entstehung des dynamischen Auftriebes von Tragflügeln. *ZAMM-Journal of Applied Mathematics and Mechanics/ Zeitschrift für Angewandte Mathematik und Mechanik*, 1925, **5**, 1–17. (in German)

[36] Küssner H G. Zusammenfassender Bericht über den instationären Auftrieb von Flügeln. *Luftfahrtforschung*, 1936, **13**, 410–424. (in German)

[37] Keenon M, Klingebiel K, Won H, Andriukov A. Development of the nano hummingbird: A tailless flapping wing micro air vehicle. *Proceedings of AIAA Aerospace Sciences Meeting including the New Horizons Forum and Aerospace Exposition*, Nashville, Tennessee, USA, 2012, 1–24.

[38] Nguyen Q V, Park H C, Goo N S, Byun D. Characteristics of a beetle's free flight and a flapping wing system that mimics beetle flight. *Journal of Bionic Engineering*, 2010, **7**, 77–86.

[39] Ma K Y, Chirarattananon P, Fuller S B, Wood R J. Controlled flight of a biologically inspired, insect-scale robot. *Science*, 2013, **340**, 603–607.

[40] Lua K B, Lai K C, Lim T T, Yeo K S. On the aerodynamic characteristics of hovering rigid and flexible hawkmoth-like wings. *Experiments in Fluids*, 2010, **49,** 1263–1291.

[41] Han J S, Kim J K, Chang J W, Han J H. An improved quasi-steady aerodynamic model for insect wings that considers movement of the center of pressure. *Bioinspiration & Biomimetics*, 2015, **10**, 1–13.

[42] Truong Q T, Phan H V, Sane S P, Park H C. Pitching moment generation in an insect-mimicking flapping-wing system. *Journal of Bionic Engineering*, 2014, **11**, 36–51.

[43] Meng X G, Sun M. Aerodynamics and vortical structures in hovering fruitflies. *Physics of Fluids*, 2015, **27**, 1–22.